

Article

# Directly-Patternable Bi<sub>2</sub>O<sub>3</sub> Nanoparticle for Polymer Nanocomposite Capacitor

Ki-Hoon Son  and Hong-Sub Lee \*

Department of Materials Science and Engineering, Kangwon National University, Chuncheon 24341, Korea; sonlee615@kangwon.ac.kr

\* Correspondence: hong-sub.lee@kangwon.ac.kr

Received: 15 July 2020; Accepted: 28 July 2020; Published: 1 August 2020



**Abstract:** A polyvinylidene fluoride (PVDF) film incorporating size-controlled, uniformly dispersed, directly patterned Bi<sub>2</sub>O<sub>3</sub> nanoparticles was developed to achieve a high-k polymer nanocomposite capacitor. The photochemical metal-organic deposition (PMOD) method was employed to form uniformly dispersed and directly patterned nanoparticles on the substrate. Bi nanoparticles were produced by spin coating a Bismuth 2-ethylhexanoate solution on a Pt substrate with UV irradiation for 1, 4, 7, and 10 min. The average diameter of nanoparticles and the number of nanoparticles per unit area (μm<sup>2</sup>) were about 30, 70, and 120 nm and 30, 30, and 31 particles/μm<sup>2</sup> for UV irradiation times of 4, 7, and 10 min, respectively. In addition, the capacitance of PVDF nanocomposite film could be controlled by the Bi<sub>2</sub>O<sub>3</sub> nanoparticle size. The PVDF nanocomposite film containing Bi<sub>2</sub>O<sub>3</sub> nanoparticles with 1, 4, 7, and 10 min UV irradiation were able to improve capacitance by about 1.4, 2.0, 2.7, and 3.4 times compared with an as-prepared PVDF film. By using a mask aligner, directly patterned Bi nanoparticles on the substrate, which had a 5 μm line width pattern, were successfully defined and demonstrated.

**Keywords:** patternable nanoparticle; bismuth oxide; polymer nanocomposite capacitor; high-K; photochemical metal-organic deposition

## 1. Introduction

Recently, miniaturization of electronic devices is the trend to manufacture ever smaller mechanical, electronic and optical products and devices. Simultaneously, high density packaging, high performance and multifunction technologies have been developed as well [1,2]. And electronic devices that are reliable, smaller, and more faster than ever would need much improved electro energy storage devices. So, several electronic devices and micro electro mechanical system (MEMS) require capacitors that show high performance. In order to apply electron energy storage device to these miniaturized devices, patterning technology must be possible and excellent dielectric properties of materials must be achieved [3,4]. By applying pattern to high dielectric materials, the device can be fabricated with more detail and density, making it suitable for miniaturization and high performance.

Dielectric materials play important roles in electric systems. Since they are essential, demand for them is high, but material improvement is important for low cost and high performance. Recently, polymer-based materials have attracted attention for flexible electronic devices. Their flexibility, low cost, fast discharge rate, low dielectric loss, and simple manufacturing process make it possible to apply them to capacitors [5–10]. Among them, polyvinylidene fluoride (PVDF) shows a relatively high permittivity ( $k = 5\text{--}10$ ), superhydrophobicity with low surface energy, remarkable mechanical strength, and chemical resistance. However, the permittivity is still not enough for high-performance electronic devices compared with inorganic compound materials such as ZrO<sub>2</sub> ( $k = 30$ ), TiO<sub>2</sub> ( $k = 90$ ), Bi<sub>2</sub>O<sub>3</sub> ( $k = 60$ ), and SrTiO<sub>3</sub> ( $k = 370$ ) [11–14]. Recent studies have shown that permittivity could be

improved several times by using single-walled carbon nanotubes or incorporating and dispersing high-k ceramic particles in PVDF [15–19]. For the high-k nanoparticle-incorporated PVDF film, uniformly dispersed, size-controlled high-k nanoparticles and synthesizing method are required, and are also the most important techniques [20]. So, the photochemical metal-organic deposition (PMOD) method was employed to obtain mass production potential, cost competitiveness and ease of processing, and to overcome difficulties in particle manufacturing and dispersion.

PMOD has usually been used for direct patterned thin films [21–23]. In this study, PMOD was applied to direct patterned nanoparticles. The PMOD method can form size-controlled, uniformly dispersed, and directly patterned nanoparticles on the substrate [24,25]. PMOD is a process that is relatively stable to humidity and temperature, since a photochemical metal-organic precursor is used as a starting material, and the chemical reaction is initiated and progressed with only UV irradiation. It is possible to obtain a nanometer-scale pattern with the PMOD process without using photoresist and an etching process. Therefore, the PMOD method has advantages such as high productivity and low cost for electronic device fabrication. Furthermore, we expect to control the nanoparticle size and density on the substrate using UV irradiation time [26,27].



The above equations describe the photochemical reaction by UV irradiation ( $L$ : ligand). The UV irradiation of the spin-coated photochemical precursor film on the substrate induces initiation and growth reactions, as shown in Figure 1a. The initiation reaction refers to a process in which Bi(III) 2-ethylhexanoate decomposes into  $\text{Bi}^{3+}$ , 2-ethylhexanoic acid,  $\text{CO}_2$ , and  $\text{C}_7\text{H}_{15}$  radical. During the continuous UV irradiation, as shown in Figure 1b,  $\text{C}_7\text{H}_{15}$  radicals involve the decomposition reaction of Bi(III) 2-ethylhexanoate into  $\text{Bi}^{3+}$ ,  $\text{CO}_2$ ,  $\text{C}_7\text{H}_{14}$ , and  $\text{C}_7\text{H}_{16}$ , after which the byproduct ( $\text{CO}_2$ ,  $\text{C}_7\text{H}_{14}$ ,  $\text{C}_7\text{H}_{16}$ ) diffuses out into the air. As a result, the decomposed  $\text{Bi}^{3+}$  cation forms  $\text{Bi}_x\text{O}_y$  nanoparticles by bonding with atmospheric oxygen on the UV-exposed area. The photochemical reaction stops at the same time as the UV irradiation ends, and the remaining photochemical precursor is removed with solvent for the patterned nanoparticles.

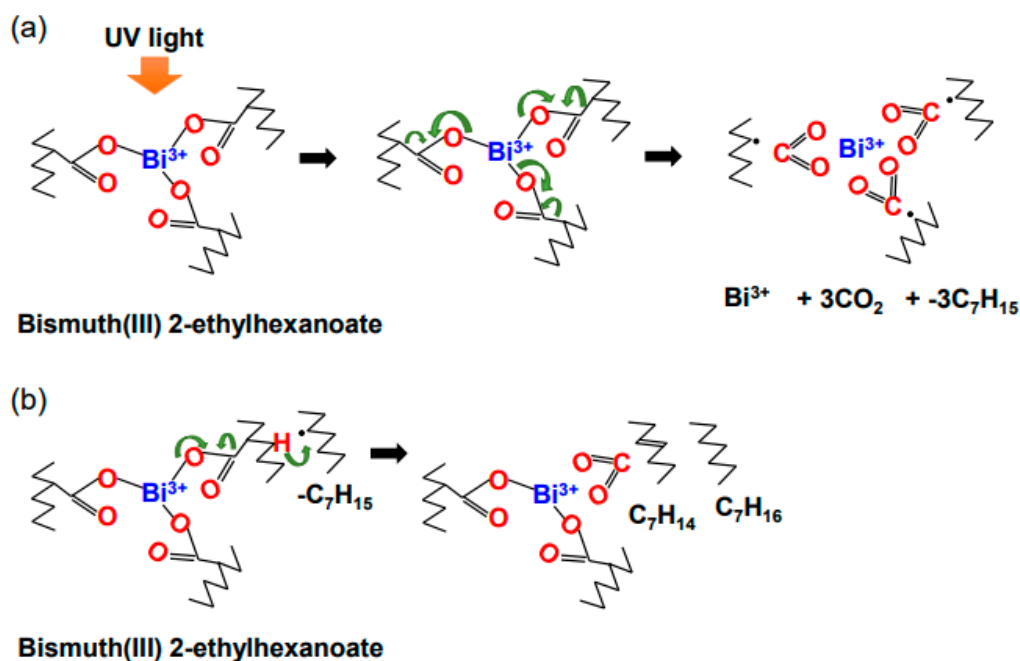
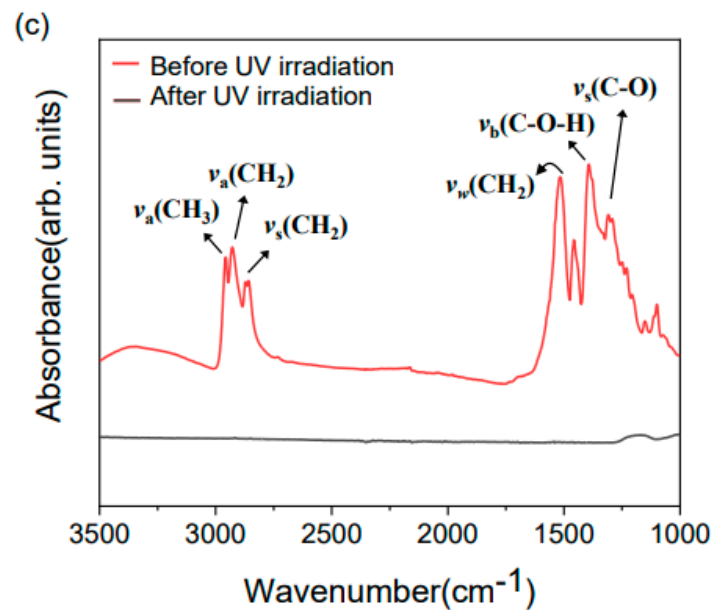


Figure 1. Cont.



**Figure 1.** Schematic diagram of (a) initiation and (b) propagation reaction of Bi(III) 2-ethylhexanoate, and (c) FR-IR spectra of spin-coated metal-organic precursor films before and after UV irradiation.

## 2. Materials and Methods

The bottom electrode Pt (75 nm)/Ti (5 nm) was deposited on a chemically clean SiO<sub>2</sub> (300 nm)/p-Si substrate using an E-beam evaporator. In addition, photochemical precursor Bismuth(III) 2-ethylhexanoate (Alfa Aesar, Ward Hill, MA, USA) was spin-coated on the prepared Pt substrate at 500 rpm for 20 s. The spin-coated photochemical precursor film was exposed by 350 W UV light using the proximity mode of the mask aligner for 0, 1, 4, 7, and 10 min, respectively. After UV irradiation, the remaining photochemical precursor and organic residue were washed out with acetone and n-hexane. FT-IR (PerkinElmer, Frontier, Waltham, MA, USA) was used to observe the photochemical reactions of Bismuth(III) 2-ethylhexanoate, and the size and density of the synthesized nanoparticles on a substrate were observed with an ultra-high-resolution scanning electron microscope (UHR-SEM) (Hitachi, S-4800, Hitachi, Tokyo, Japan). To form alpha phase Bi<sub>2</sub>O<sub>3</sub>, we annealed the Bi<sub>x</sub>O<sub>y</sub> nanoparticles in a tube furnace at 300 °C for 5 h. Then we performed XRD (PANalytical, X'Pert PRO MPD, Almelo, the Netherlands) measurement of the samples before and after heat treatment to investigate the phase formation of Bi<sub>2</sub>O<sub>3</sub> and crystal structure. PVDF (Sigma Aldrich, St. Louis, MO, USA) was dissolved in N-Methyl-2-pyrrolidone (Daejung, Siheung, Korea) with 12 wt.% and mixed in a stirrer for 12 h. The PVDF solution was spin-coated on Bi<sub>2</sub>O<sub>3</sub> nanoparticles at 3500 rpm for 20 s and heat treated at 90 °C for 15 min on a hot plate (solvent evaporation), which formed 350 nm thick PVDF film. An atomic force microscope (Park systems, XE-100, Suwon, Korea) was used to observe the Bi<sub>2</sub>O<sub>3</sub> nanoparticle- incorporated PVDF film. The 100 nm thick, 200 μm diameter Pt top electrode was deposited using a shadow mask and an E-beam evaporator. The dielectric constant of the completed device was measured at 10<sup>5</sup> Hz using a Wayne Kerr LCR Meter 4100.

## 3. Results and Discussions

Figure 1c shows the FT-IR spectrum before and after UV irradiation of the spin-coated Bi(III) 2-ethylhexanoate precursor film on a SiO<sub>2</sub> (200 nm)/p-Si substrate. In the case of unexposed film, an alkyl group (-CH<sub>3</sub>) and alkene group (-CH<sub>2</sub>) were observed at 2958, 2932 and 2860 cm<sup>-1</sup>. Absorption peaks associated with C-O symmetric stretching, C-O-H bending vibration, and stretching vibrations CH<sub>2</sub> of ethyl hexanoate ligand occurred between 1100 and 1700 cm<sup>-1</sup> [28–30]. The nucleation and growth progressed only during UV irradiation, and after UV irradiation, the remaining photochemical

precursor and organic residue were completely removed by acetone and n-hexane, as shown in Figure 1c.  $\text{Bi}_x\text{O}_y$  nanoparticles only remained in the UV-exposed areas of the substrate.

This study used UV irradiation time as the control factor to tune the nanoparticle size, and Figure 2 shows SEM images of bismuth nanoparticles according to UV irradiation time. Figure 2a–d correspond to UV irradiation times of 1, 4, 7, and 10 min, respectively. As shown in Figure 2e, nanoparticles size increased linearly with the increase in UV irradiation time, and the number of nanoparticles per unit area did not increase. In the case of the 1 min (exposure time) sample, we could not perform meaningful measurements for nanoparticle size and the number of nanoparticles, as shown in Figure 2a, since 1 min (UV irradiation time) was not enough time to form nanoparticles on the substrate. The average diameter of the nanoparticles and the number of nanoparticles per unit area ( $\mu\text{m}^2$ ) were about 30, 70, and 120 nm and 30, 30, and 31 particles/ $\mu\text{m}^2$  for UV irradiation times of 4, 7, and 10 min, respectively. These results show that we can directly synthesize patterned nanoparticles on a substrate using the PMOD method and easily control nanoparticle size and density using UV irradiation time.

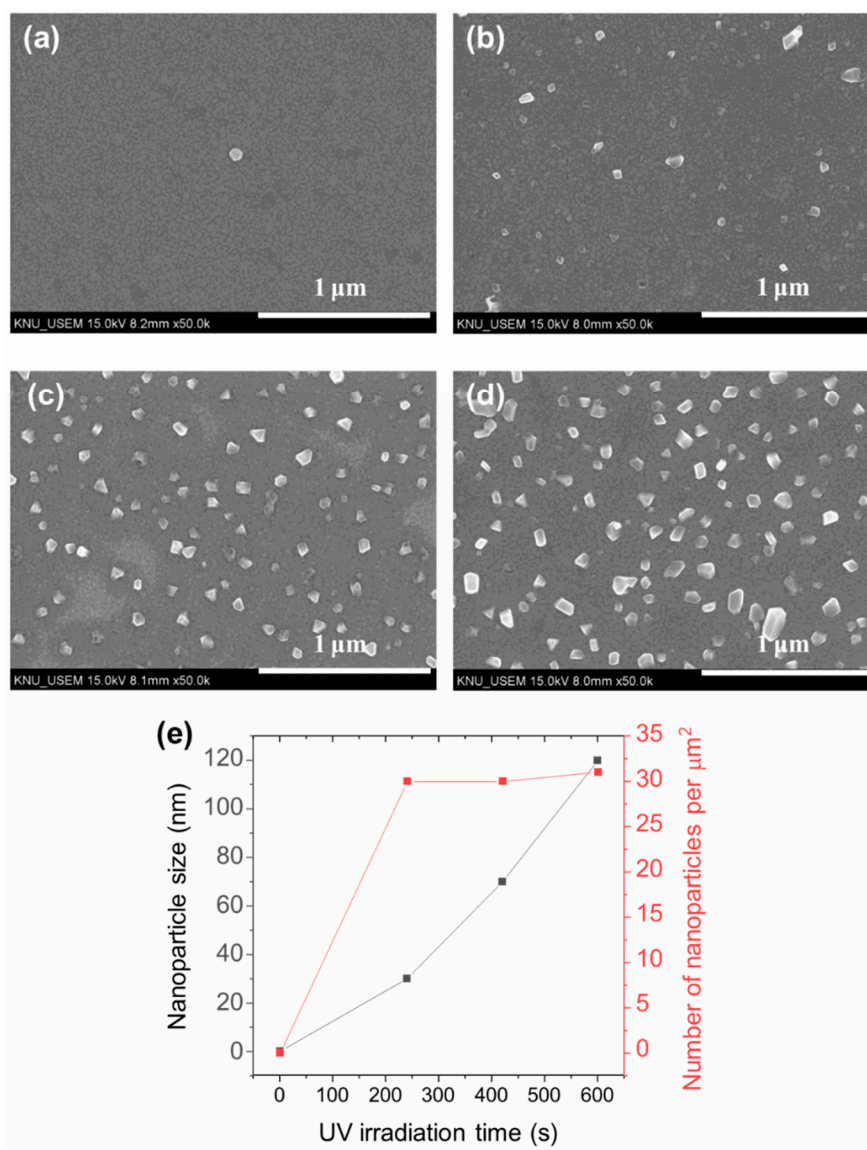


**Figure 2.** SEM images of Bi nanoparticles according to UV irradiation time (a) 1min, (b) 4 min, (c) 7 min, (d) 10 min. (e) The average nanoparticles diameter and the number of nanoparticles per unit area versus UV irradiation time.

Figure 3 shows the x-ray diffraction patterns of an as-prepared sample and 300 °C annealed sample. Interestingly, the as-prepared sample shows a diffraction pattern of bismuth metal. In the PMOD process for directly patterned thin film, the product material right after UV irradiation is usually an amorphous metal oxide [31–35].

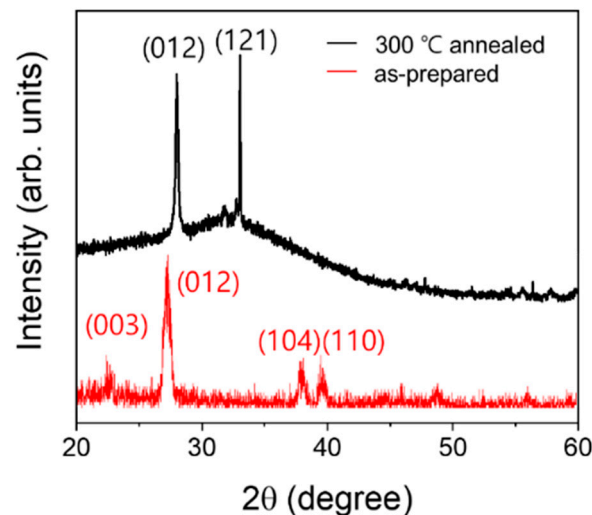
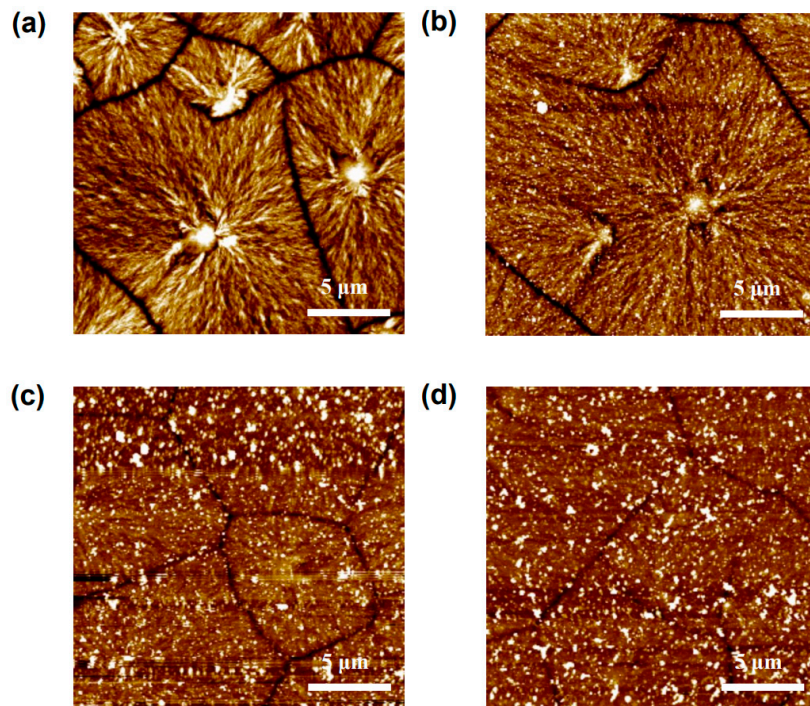


Figure 3. X-ray diffraction patterns of as-prepared and 300 °C annealed samples.

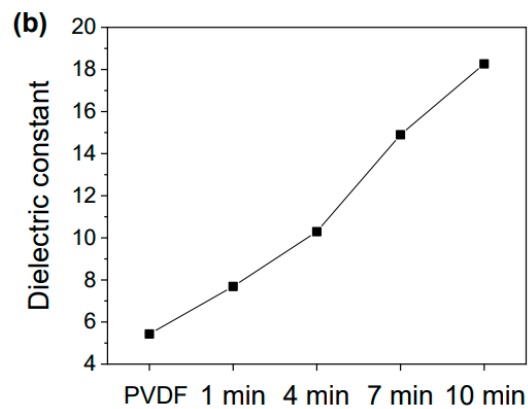
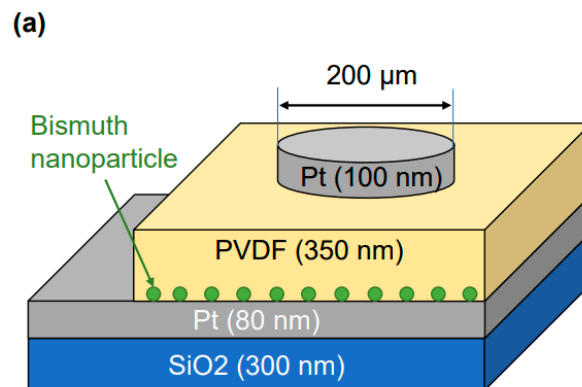
However, in this study, the bismuth nanoparticles were synthesized as a form of crystallized metal, as shown in Figure 3. (The polyhedron shapes of nanoparticles were observed in the SEM image of Figure 2). We suppose that the short UV irradiation time and the thick precursor film might minimize exposure of the bismuth nuclei to atmospheric oxygen during nucleation and growth, which prevents the oxidation of bismuth metal nuclei and facilitates crystallization and growth. Therefore, the present study annealed the as-prepared sample at 300 °C under atmosphere to form high-k dielectric material  $\text{Bi}_2\text{O}_3$ . As shown in Figure 3, this study obtained an alpha  $\text{Bi}_2\text{O}_3$  phase (JCPDS 76-7130) from the annealing process. After the annealing process, the oxidized  $\text{Bi}_2\text{O}_3$  nanoparticles showed a volume expansion of about 60% compared with bismuth metal nanoparticles.

Figure 4 shows the AFM images of  $\text{Bi}_2\text{O}_3$  nanoparticle-incorporated PVDF films according to UV irradiation time. As shown in Figure 4, the nanoparticle-incorporated PVDF films were formed well on the uniformly dispersed  $\text{Bi}_2\text{O}_3$  nanoparticles. The root mean square (RMS) values of surface morphology were 6.05, 8.43, 24.45, and 29.49 nm for 1, 4, 7, and 10 min samples, respectively. The increasing RMS value reflects the increase in  $\text{Bi}_2\text{O}_3$  nanoparticle size. The RMS values, average nanoparticle size, and density in the AFM images agree well with the SEM image in Figure 2.

Figure 5 shows a schematic diagram of the  $\text{Bi}_2\text{O}_3$  nanoparticle-incorporated PVDF capacitor device and measured dielectric constant data for 0, 1, 4, 7, and 10 min samples. The measured dielectric constants of PVDF reference film (without  $\text{Bi}_2\text{O}_3$  nanoparticles) at 1, 4, 7, and 10 min were 5.43, 7.69, 10.29, 14.90, and 18.27, respectively. The dielectric constant of the nanoparticle-incorporated PVDF films also increased linearly with the increase in nanoparticle size and density. Based on the measured dielectric constant, it is believed that  $\text{Bi}_2\text{O}_3$  nanoparticles were also formed in the UV irradiation time 1 min sample.



**Figure 4.** AFM image after PVDF deposition on (a) 1, (b) 4, (c) 7, and (d) 10 min samples.



**Figure 5.** (a) Schematic diagram and (b) the dielectric constant of the  $\text{Bi}_2\text{O}_3$  nanoparticle incorporated PVDF capacitor devices.

Finally, we could obtain size-controlled, uniformly dispersed, directly patternable nanoparticle-incorporated PVDF films that have improved permittivity. Figure 6 shows a microscope image of directly patterned  $\text{Bi}_2\text{O}_3$  nanoparticles on an  $\text{SiO}_2$  substrate that has 5  $\mu\text{m}$  line width. The direct patterning process was performed by removing the area that was not exposed to UV light by rinsing it with solvent after the exposure of the films through a photomask. In the optical microscope image, the blueish area indicates the  $\text{Bi}_2\text{O}_3$  nanoparticle region. As shown in the line patterned region, micron-size direct patterning was well defined by lithographic patterning using PMOD.

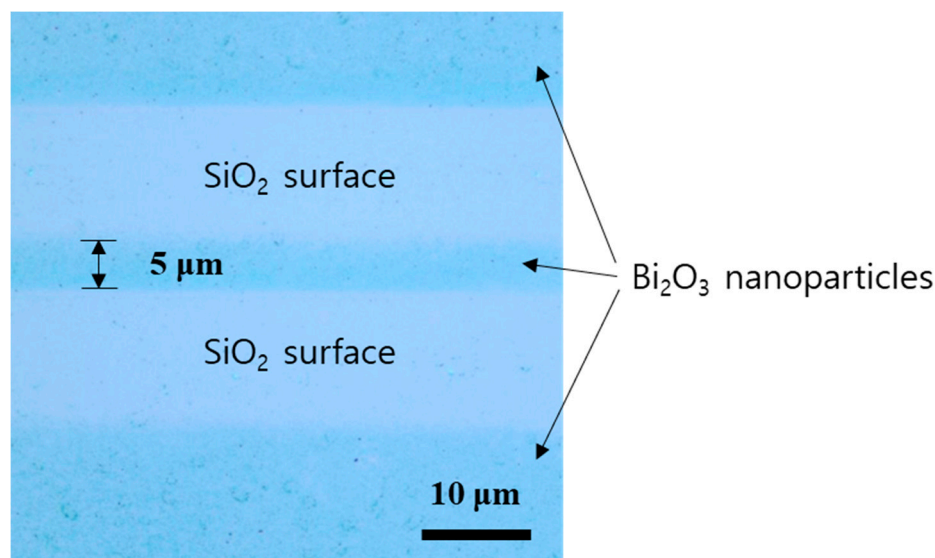


**Figure 6.** Optical microscope image of directly-patterned  $\text{Bi}_2\text{O}_3$  nanoparticles on  $\text{SiO}_2$  substrate.

#### 4. Conclusions

This study successfully demonstrated a PVDF nanocomposite capacitor incorporating size-controlled, uniformly dispersed, directly patterned  $\text{Bi}_2\text{O}_3$  nanoparticles using the PMOD method. The nanoparticle size could be easily controlled since a photochemical reaction was initiated and progressed with only UV irradiation. The average diameter and density of synthesized nanoparticles increased linearly with an increase in UV irradiation time. From the PMOD nanoparticle synthesis, we could obtain a uniformly dispersed  $\text{Bi}_2\text{O}_3$  nanoparticle-incorporated PVDF dielectric film, and the permittivity of the films also increased linearly with the increase in nanoparticle size and density. Furthermore, directly patterned alpha phase  $\text{Bi}_2\text{O}_3$  nanoparticles could be formed on the substrate using a mask aligner. These results indicate that the PMOD nanoparticle synthesis method can be applied to nanoelectronic devices from various photosensitive metal-organic precursors, and with PMOD, it was confirmed that metal nanoparticles can be produced, not only metal oxide nanoparticles. It is expected to be able to apply to metal nanoparticle synthesis and device manufacturing processes. In addition, the difficulty and cost of this process were relatively low, so it could be easily produced in a short time.

**Author Contributions:** Conceptualization, K.-H.S. and H.-S.L.; methodology, K.-H.S. and H.-S.L.; software, K.-H.S. and H.-S.L.; validation, K.-H.S. and H.-S.L.; formal analysis, K.-H.S. and H.-S.L.; investigation, K.-H.S. and H.-S.L.; resources, H.-S.L.; data curation, K.-H.S.; writing—original draft preparation, K.-H.S.; writing—review and editing, H.-S.L.; visualization, K.-H.S. and H.-S.L.; supervision, H.-S.L.; project administration, H.-S.L.; funding acquisition, H.-S.L. All authors have read and agreed to the published version of the manuscript.

**Funding:** This work was supported by the National Research Foundation of Korea (NRF) grant funded by the Korea government Ministry of Science and ICT (MSIT) (2019R1F1A1059637) and the Ministry of Trade, Industry & Energy (MOTIE, Korea) under Industrial Strategic Technology Development Program. No. 10068075, ‘Development of Mott-transition based forming-less non-volatile resistive switching memory & array’.

**Conflicts of Interest:** The authors declare no conflict of interest.

## References

1. Zhang, P.; Xue, S.; Wang, J. New challenges of miniaturization of electronic devices: Electromigration and thermomigration in lead-free solder joints. *Mater. Des.* **2020**, *192*, 108726. [[CrossRef](#)]
2. Annuar, S.; Mahmoodian, R.; Hamdi, M.; Tu, K.N. Intermetallic compounds in 3D integrated circuits technology: A brief review. *Sci. Technol. Adv. Mater* **2017**, *18*, 693–703. [[CrossRef](#)]
3. Hwang, J.S.; Kim, W.S.; Park, H.H.; Kim, T.S. The effect of intermediate anneal on the ferroelectric properties of direct-patternable PZT films. *Sens. Actuators A Phys.* **2005**, *117*, 137–142. [[CrossRef](#)]
4. Grove, T.T.; Masters, M.F.; Miers, R.E. Determining dielectric constants using a parallel plate capacitor. *Am. J. Phys.* **2005**, *73*, 52–56. [[CrossRef](#)]
5. Baojin, C.; Xin, Z.; Kailiang, R.; Bret, N.; Minren, L.; Qing, W.; Bauer, F.; Zhang, Q.M. A dielectric polymer with high electric energy density and fast discharge speed. *Science* **2006**, *313*, 334–336.
6. Xie, L.Y.; Huang, X.Y.; Jiang, P.K.; Huang, Y.H.; Yang, K. Core-shell structured hyperbranched aromatic polyamide/BaTiO<sub>3</sub> hybrid filler for poly (vinylidene fluoride-trifluoroethylene -chlorofluoroethylene) nanocomposites with the dielectric constant comparable to that of percolative composites. *Appl. Mater. Interface* **2013**, *5*, 1747–1756. [[CrossRef](#)]
7. Joyce, D.M.; Ouchen, F.; Grote, J.G. Re-engineering the polymer capacitor, layer by layer. *Adv. Energy Mater.* **2016**, *6*, 1600676. [[CrossRef](#)]
8. Tan, D.; Zhang, L.; Chen, Q.; Irwin, P. High-temperature capacitor polymer films. *J. Electron. Mater.* **2014**, *43*, 4569–4575. [[CrossRef](#)]
9. Han, W.J.; Lee, H.S.; Bangi, U.-K.H.; Yoo, B.W.; Park, H.H. Dielectric properties of poly(4-vinylphenol) with embedded PbO nanoparticles. *Polym. Adv. Technol.* **2015**, *27*, 245–249. [[CrossRef](#)]
10. Mukhin, N.; Sokolova, I.; Chigirev, D.; Rudaja, L.; Lebedeva, G.; Kastro, R.; Bol'shakov, M.; Schmidt, M.-P.; Hirsch, S. Composite ferroelectric coatings based on a heat-resistant polybenzoxazole polymer matrix. *Coatings* **2020**, *10*, 286. [[CrossRef](#)]
11. Xie, J.; Zhu, Z.; Tao, H.; Zhou, S.; Liang, Z.; Li, Z.; Yao, R.; Wang, Y.; Ning, H.; Peng, J. Research progress of high dielectric constant zirconia-based materials for gate dielectric application. *Coatings* **2020**, *10*, 698. [[CrossRef](#)]
12. Fröhlich, K.; Ľapajna, M.; Rosová, A.; Dobročka, E.; Hušeková, K.; Aarik, J.; Aidla, A. Growth of high-dielectric-constant TiO films in capacitors with RuO electrodes. *Electrochem. Solid-State Lett.* **2008**, *11*, G19.
13. Halford, J.H.; Hacker, H. Dielectric properties of bismuth trioxide thin films. *Thin Solid Film.* **1969**, *4*, 265–279. [[CrossRef](#)]
14. Komatsu, S.; Abe, K.; Fukushima, N. Effects of ambient gas on dielectric constant of sputtered SrTiO<sub>3</sub> epitaxial thin films. *Jpn. J. Appl. Phys.* **1998**, *37*, 5651–5654. [[CrossRef](#)]
15. Valipour, P.; Ghasemi, S.E.; Khosravani, M.R.; Ganji, D.D. Theoretical analysis on nonlinear vibration of fluid flow in single-walled carbon nanotube. *J. Theor. Appl. Phys.* **2016**, *10*, 211–218. [[CrossRef](#)]
16. Jiang, J.; Wang, L.; Zhang, Y. Vibration of single-walled carbon nanotubes with elastic boundary conditions. *Int. J. Mech. Sci.* **2017**, *122*, 156–166. [[CrossRef](#)]
17. Yang, K.; Huang, X.; Huang, Y.; Xie, L.; Jiang, P. Fluoro-polymer@BaTiO<sub>3</sub> hybrid nanoparticles prepared via RAFT polymerization: Toward ferroelectric polymer nanocomposites with high dielectric constant and low dielectric loss for energy storage application. *Chem. Mater.* **2013**, *25*, 2327–2338. [[CrossRef](#)]
18. Singh, D.; Singh, N.; Garg, A.; Gupta, R.K. Engineered thiol anchored Au-BaTiO<sub>3</sub>/PVDF polymer nanocomposite as efficient dielectric for electronic applications. *Compos. Sci. Technol.* **2019**, *174*, 158–168.
19. Wang, L.; Dang, Z.M. Carbon nanotube composites with high dielectric constant at low percolation threshold. *Appl. Phys. Lett.* **2005**, *87*, 042903. [[CrossRef](#)]
20. Hong, R.Y.; Chen, Q. Dispersion of inorganic nanoparticles in polymer matrices: Challenges and solutions. *Adv. Polym. Sci.* **2014**, *267*, 1–38.
21. Park, H.H.; Park, H.H.; Hill, R.H. Direct-patterning of SnO<sub>2</sub> thin film by photochemical metal-organic deposition. *Sens. Actuators A* **2006**, *132*, 429–433. [[CrossRef](#)]
22. Lee, H.S.; Choi, H.J.; Chung, S.W.; Park, H.H. Effect of SrTiO<sub>3</sub> buffer layer on the phase formation and properties of direct-patternable BiFeO<sub>3</sub> thin films fabricated using photochemical metal-organic deposition. *Ceram. Soc. Jpn.* **2010**, *118*, 1024–1027. [[CrossRef](#)]

23. BuonoCore, G.E.; Cabello, G.; Klahn, A.H.; Lucero, A.; Nuñez, M.V.; Torrejón, B.; Castillo, C. Growth and characterization of molybdenum oxide thin films prepared by photochemical metal–organic deposition (PMOD). *Polyhedron* **2010**, *29*, 1551–1554. [[CrossRef](#)]
24. Zhu, H.J.; Hill, R.H. The photochemical metal organic deposition of manganese oxide films from films of manganese(II) 2-ethylhexanoate: A mechanistic study. *J. Non-Cryst. Solids* **2002**, *311*, 174–184. [[CrossRef](#)]
25. Wu, B.E.; Chiang, C.Y. Photochemical metal organic deposition of FeO<sub>x</sub> catalyst on BiVO<sub>4</sub> for improving solar-driven water oxidation efficiency. *J. Taiwan Inst. Chem. Eng.* **2017**, *80*, 1014–1021. [[CrossRef](#)]
26. Andronic, L.S.; Hill, R.H. The mechanism of the photochemical metal organic deposition of lead oxide films from thin films of lead (II) 2-ethylhexanoate. *J. Photochem. Photobiol. A Chem.* **2002**, *152*, 259–265. [[CrossRef](#)]
27. Tradel, S.; Li, G.; Zhang, X.; Hill, R.H. Positive and Negative Lithography by Photochemical Metalorganic Deposition from Metal 2-ethylhexanoates. *J. Photopolym. Sci. Technol.* **2006**, *19*, 467–475. [[CrossRef](#)]
28. Yang, J.; Xie, T.; Liu, C.; Xu, L. Facile fabrication of dumbbell-Like β-Bi<sub>2</sub>O<sub>3</sub>/graphene nanocomposites and their highly efficient photocatalytic activity. *Materials* **2018**, *11*, 1359. [[CrossRef](#)]
29. Liu, M.; Zhang, L.; Wang, K.; Zheng, Z. Low temperature synthesis of δ-Bi<sub>2</sub>O<sub>3</sub> solid spheres and their conversion to hierarchical BiOI nests via the Kirkendall effect. *CrystEngComm* **2011**, *13*, 5460. [[CrossRef](#)]
30. Epifani, M.; Tang, P.Y.; Genç, A.; Morante, J.R.; Arbiol, J.; Díaz, R.; Wicker, S. The ethylhexanoate route to metal oxide nanocrystals: Synthesis of CoO nanooctahedra from Co(II) 2-Ethylhexanoate. *Eur. J. Inorg. Chem.* **2016**, *24*, 3963–3968. [[CrossRef](#)]
31. Shi, Y.; Li, G.; Hill, R.H. Preparation of nanocomposite thin films by sol-gel and photochemical metal–organic deposition of Ba<sub>0.5</sub>Sr<sub>0.5</sub>TiO<sub>3</sub> and PbZr<sub>0.48</sub>Ti<sub>0.52</sub>O<sub>3</sub>. *Mater. Sci. Semicond. Process.* **1999**, *2*, 297–301. [[CrossRef](#)]
32. Trudel, S.; Jones, C.H.W.; Hill, R.H. Magnetic properties of nanocrystalline iron oxide/amorphous manganese oxide nanocomposite thin films prepared via photochemical metal-organic deposition. *J. Mater. Chem.* **2007**, *17*, 2206. [[CrossRef](#)]
33. Chen, C.W.; Chiang, C.Y. Molybdenum-containing amorphous metal oxide catalysts for oxygen evolution reaction. *Int. J. Hydrog. Energy* **2017**, *42*, 29773–29780. [[CrossRef](#)]
34. Pan, L.; Wang, Q.; Li, Y.; Zhang, C. Amorphous cobalt-cerium binary metal oxides as high performance electrocatalyst for oxygen evolution reaction. *J. Catal* **2020**, *384*, 14–21. [[CrossRef](#)]
35. Ligang, L.; Shao, Q.; Huang, X. Amorphous Oxide Nanostructures for Advanced Electrocatalysis. *Chem. Eur. J.* **2019**, *25*, 1–19.



© 2020 by the authors. Licensee MDPI, Basel, Switzerland. This article is an open access article distributed under the terms and conditions of the Creative Commons Attribution (CC BY) license (<http://creativecommons.org/licenses/by/4.0/>).